

1 The Orbiting Carbon Observatory-2: First 18 months of Science Data Products

2

3 Annmarie Eldering¹, Chris W. O'Dell², Paul O. Wennberg³, David Crisp¹, Michael R. Gunson¹, Camille Viatte³,
4 Charles Avis¹, Amy Braverman¹, Rebecca Castano¹, Albert Chang¹, Lars Chapsky¹, Cecilia Cheng¹, Brian
5 Connor⁴, Lan Dang¹, Gary Doran¹, Brendan Fisher¹, Christian Frankenberg^{1,2}, Dejian Fu¹, Robert Granat¹,
6 Jonathan Hobbs¹, Richard A. M. Lee¹, Lukas Mandrake¹, James McDuffie¹, Charles E. Miller¹, Vicky Myers¹,
7 Vijay Natraj¹, Denis O'Brien², Gregory B. Osterman¹, Fabiano Oyafuso¹, Vivienne H. Payne¹, Harold R. Pollock¹,
8 Igor Polonsky^{3,5}, Coleen M. Roehl³, Robert Rosenberg¹, Florian Schwandner¹, Mike Smyth¹, Vivian Tang¹,
9 Thomas E. Taylor², Cathy To¹, Debra Wunch^{3,6}, Jan Yoshimizu¹

Deleted: ⁴

Deleted: ⁵

10 [1] Jet Propulsion Laboratory, California Institute of Technology, Pasadena, CA

11 [2] Cooperative Institute for Research in the Atmosphere, Colorado State University, Fort Collins, CO

12 [3] Department of Geology and Planetary Sciences, California Institute of Technology, Pasadena, CA

13 [\[4\] BC Scientific Consulting, Stony Brook, NY, USA](#)

14 [\[5\] currently at Atmospheric and Environmental Research, Inc., Lexington, MA](#)

Deleted: 4

15 [\[6\] as of December 2015, University of Toronto, Department of Physics, Toronto, Canada](#)

16 Correspondence to: A. Eldering (Annmarie.Eldering@jpl.nasa.gov)

17

18

19 Abstract

20 The Orbiting Carbon Observatory-2 (OCO-2) is the first National Aeronautics and Space Administration (NASA) satellite designed
21 to measure atmospheric carbon dioxide (CO₂) with the accuracy, resolution, and coverage needed to quantify CO₂ fluxes (sources
22 and sinks) on regional scales. OCO-2 was successfully launched on 2 July 2014, and [has gathered more than two years of](#)
23 [observations. The v7/v7R operational data products from September 2014 to January 2016 are discussed here.](#) On monthly time
24 scales, 7 to 12% of these measurements are sufficiently cloud and aerosol free to yield estimates of the column-averaged
25 atmospheric CO₂ dry air mole fraction, X_{CO₂}, that pass all quality tests. During the first year of operations, the observing strategy,
26 instrument calibration, and retrieval algorithm were optimized to improve both the data yield and the accuracy of the products.
27 With these changes, global maps of X_{CO₂} derived from the OCO-2 data are revealing some of the most robust features of the
28 atmospheric carbon cycle. This includes X_{CO₂} enhancements co-located with intense fossil fuel emissions in eastern U.S. and
29 eastern China, which are most obvious between October and December, when the north-south X_{CO₂} gradient is small. Enhanced
30 X_{CO₂} coincident with biomass burning in the Amazon, central Africa, and Indonesia is also evident in this season. In May and June,
31 when the north-south X_{CO₂} gradient is largest, these sources are less apparent in global maps. During this part of the year, OCO-2
32 maps show a more than 10 ppm reduction in X_{CO₂} across the northern hemisphere, as photosynthesis by the land biosphere rapidly
33 absorbs CO₂. As the carbon cycle science community continues to analyze these OCO-2 data, information on regional-scale sources
34 (emitters) and sinks (absorbers) which impart X_{CO₂} changes on the order of 1 ppm, as well as far more subtle features, will emerge
35 from this high resolution, global data set.

Deleted: joined the 705 km Afternoon Constellation on 3 August 2014

1

2 1 Introduction

3 Human activities including fossil fuel combustion, cement production, and deforestation are now adding almost 40 billion tons of
4 carbon dioxide (CO₂) to the atmosphere each year (c.f. Le Quéré et al., 2015). If all of this CO₂ remained in the atmosphere, the
5 atmospheric CO₂ concentration would increase by more than one percent (1%) per year. Interestingly, precise measurements
6 collected by a growing global network of greenhouse gas monitoring stations over the past 60 years indicate that less than half of
7 this CO₂ remains airborne (Dlugokencky and Tans, 2015) The rest is being absorbed by the oceans and the land biosphere.
8 Measurements of the partial pressure of CO₂ in seawater collected over this period indicate that almost a quarter of the CO₂ emitted
9 by human activities is being absorbed by the ocean (c.f. Takahashi et al. 2009), where it contributes to ocean acidification. For
10 mass balance reasons, another 10 billion tons of CO₂ must be absorbed by processes on land, whose identity and location are less
11 well understood. Some studies have attributed this absorption to tropical (Schimel et al., 2015), or Eurasian temperate (Reuter et
12 al., 2014) forests, while others indicate that these areas are just as likely to be net sources as net sinks of CO₂ (Chevallier et al.,
13 2014). The efficiency of these natural land and ocean sinks also appears to vary dramatically from year to year (Le Quéré et al.,
14 2015). Some years, they absorb CO₂ equivalent to almost all of that emitted by human activities, while in other years, they absorb
15 very little. Because the identity, location, and processes controlling these natural sinks are not well constrained, it is not clear that
16 they will continue to reduce the rate of atmospheric CO₂ buildup by half in the future (Schimel et al., 2015). This introduces a
17 major source of uncertainty in predictions of the rate of future CO₂ increases, and their effect on the climate (Friedlingstein et al.,
18 2006; Arora et al., 2013).

19 Measurements from the network of ground-based greenhouse gas stations accurately track the global atmospheric CO₂ budget and
20 its trends. Remote sensing of the column-averaged CO₂ dry air mole fraction (X_{CO_2}) from space is intended to provide finer spatial
21 coverage enabling smaller scale *sources* emitting CO₂ into the atmosphere and natural *sinks* absorbing this gas at the Earth's surface
22 to be better quantified. Surface weighted X_{CO_2} estimates can be retrieved from high resolution spectroscopic observations of
23 reflected sunlight in near infrared CO₂ and O₂ bands (c.f. Rayner and O'Brien, 2001; Crisp et al., 2004; Buchwitz et al., 2006;
24 O'Dell et al., 2012). This is a challenging space-based remote sensing observation because even the largest regional CO₂ sources
25 and sinks produce changes in the background X_{CO_2} distribution no larger than 2%, and most are smaller than 0.25% (1 part per
26 million (ppm) out of the background 400 ppm) (c.f. Miller et al., 2007).

27 The European Space Agency (ESA) EnviSat SCanning Imaging Absorption SpectroMeter for Atmospheric CHartography
28 (SCIAMACHY) (Burrows et al., 1995) and Japanese Greenhouse Gases Observing Satellite (GOSAT) Thermal And Near infrared
29 Sensor for carbon Observation Fourier Transform Spectrometer (TANSO-FTS) (Nakajima et al., 2010) were the first satellite
30 instruments designed to exploit this measurement approach. SCIAMACHY enabled retrieval of column averaged CO₂ and methane
31 (X_{CH_4}) measurements over the sunlit hemisphere from 2002 to 2012. Spectra from TANSO-FTS have been used to produce X_{CO_2}
32 and X_{CH_4} observations since April 2009. These data have provided an important proof of concept, and are beginning to yield new
33 insights into the carbon cycle (Feng et al., 2016; Guerlet et al., 2013; Wunch et al., 2013; Schneising et al., 2014), but improvements
34 in sensitivity, resolution, and coverage are still needed.

35 The Orbiting Carbon Observatory-2 (OCO-2) is the first NASA satellite designed to measure atmospheric CO₂ columns with the
36 accuracy, resolution, and coverage needed to detect CO₂ sources and sinks on regional scales over the globe. OCO-2 is a
37 replacement for the Orbiting Carbon Observatory (Crisp et al., 2004, 2008) which was lost in 2009, when its launch vehicle
38 malfunctioned and failed to reach orbit. OCO-2 was successfully launched from Vandenberg Air Force Base in California on July
39 2, 2014. Since September 6th of 2014, this instrument has been routinely returning almost one million soundings each day over the

1 sunlit hemisphere. Optically thick clouds and aerosols preclude observations of the full atmospheric column, but 7 to 12% of these
2 soundings are sufficiently cloud free to yield full-column estimates of X_{CO_2} with single-sounding random errors between 0.5 and
3 1 ppm at solar zenith angles as large as 70 degrees.

4 Here we provide a brief introduction to the instrument and the mission operations to date, highlighting the global coverage,
5 resolution, and precision of the dataset. We describe the overall flow of data in section 4 and some key results in terms of data
6 quantity, quality, and features, with discussions of X_{CO_2} (section 4.3.1), data quality indicators (section 4.3.3 and 4.3.4), and overall
7 data density (section 4.3.5). The trends in X_{CO_2} in space and time as seen from OCO-2 are discussed in section 5. This paper is one
8 of a number of papers describing the OCO-2 mission and its early results. On-orbit calibration and validation of the Level-1
9 radiances are described in Crisp et al. (2016ab). Details of the X_{CO_2} retrieval algorithm, including filtering and bias correction, are
10 given in O'Dell et al. (2016), while the validation of X_{CO_2} via comparisons to the TCCON network are given in Wunch et al.
11 (2016). Finally, analysis of the Solar-Induced Fluorescence (SIF) product derived from OCO-2's Oxygen-A band is described in
12 Sun et al. (2016). Interested readers are advised to consult these references for details.

13

14

15 **2 The instrument**

16 The instrument of OCO-2 is a three-band spectrometer, which measures reflected sunlight in three separate bands. The oxygen A-
17 band (ABO2) measures absorption by molecular oxygen near 0.76 μm , while two carbon dioxide bands, labeled here as the weak
18 and strong CO_2 bands (WCO2 and SCO2 hereafter), are located near 1.6 and 2.0 μm , respectively. The instrument has 1016 spectral
19 elements in each band, and 160 pixels are averaged in groups of ~ 20 along the slit, creating eight spatial footprints. The instrument
20 field of view creates footprints that are nominally 1.25 km in width, and the spacecraft motion spans ~ 2.4 km of the ground in the
21 0.33 seconds of integration time. The spacecraft rotates along the orbit, maintaining a constant angle between the plane defined by
22 the instrument, the point observed on the ground, and the sun. As a result, the footprint shapes change during the orbit, from [very](#)
23 [narrow and long near the equator, to smaller and smaller aspect ratios, \(approaching rectangular footprints\) with increasing latitudes](#)
24 [\(see details in Crisp et al., 2016b\)](#). The rate of data collection results in approximately 1 million sets of 3 band measurements per
25 day.

Deleted: nearly rectangular to very narrow swaths

26 The OCO-2 instrument collects data over very narrow spectral ranges, with a resolving power ($\lambda/\Delta\lambda$) of roughly 19,000:1 in each
27 band that reveals the trace gas spectral absorption lines. The spectral ranges for the O_2 -A band, weak CO_2 , and strong CO_2 are
28 0.7576 to 0.7726 microns, 1.5906 to 1.6218 microns, and 2.0431 to 2.0834 microns, respectively. Details of the spectral and
29 radiometric calibration of the instrument are reported in Lee et al. (2016) and Rosenberg et al. (2016), respectively. On-orbit
30 instrument performance is described in detail in Crisp et al. (2016a). Coincident measurements from the three channels are
31 combined into "soundings" that are analysed with a "full-physics" retrieval algorithm to yield estimates of X_{CO_2} and other
32 geophysical quantities (c.f. Boesch et al., 2006, 2011; O'Dell et al., 2012, 2016; Crisp et al., 2012).

33

34

35 **3 The observatory in space**

36 The OCO-2 observatory was launched successfully from Vandenberg Air Force Base in California on July 2nd, 2014 at 2:56 am
37 Pacific Daylight Time. During the 10 days following launch, the spacecraft team completed a functional check of both the

1 observatory and the instrument. The observatory was then maneuvered into its position in the 705 km Afternoon Constellation,
2 also called the A-train, arriving on August 3rd, 2014. A number of atmospheric remote-sensing satellites fly in coordination in this
3 constellation, such as the Moderate Resolution Imaging Spectrometer (MODIS) and Cloud-Aerosol Lidar with Orthogonal
4 Polarization (CALIOP) which can be used for cross comparisons of clouds and radiances. After achieving the operational orbit,
5 the instrument and focal planes were brought to and stabilized at their operational temperatures. During the more extensive in-
6 orbit-checkout (IOC) of the instrument, measurements were collected to refine the geometric, radiometric, and spectral calibration.
7 On August 6, 2014, the first spectral data were collected with the instrument at operating temperatures, and processed with
8 calibration parameters from pre-launch calibration experiments. As reported in Basilio et al. (2014) this data showed high resolution
9 with high signal to noise characteristics similar to the prelaunch measurements. Another critical activity during the IOC were lunar
10 measurements that were used, in combination with data from coastal crossings, to determine the alignment of the spectrometers
11 and derive the updated pointing coefficients. Calibration data collected during IOC were used to update the instrument gain
12 coefficients, dark correction, and to update the map of bad pixels on the focal plane. This was completed on September 5, 2014.
13 Data after that date is considered scientifically usable, as the instrument temperatures were stable, and the key radiometric
14 parameters were up to date. The OCO-2 mission formally ended the IOC period on October 12, 2014.

15 As of the summer of 2016, the instrument and spacecraft are performing extremely well, and data collection continues. Crisp et al.
16 (2016ab) provides details of data interruptions, which have been primarily driven by instrument operations.

17

18 **3.1 The observing strategy**

19 The observing strategy of the OCO-2 mission evolved over the first year. Initially, the strategy was to collect 16 days of nadir data,
20 collecting data by measuring directly below the spacecraft, followed by 16 days of glint measurements, where the instrument is
21 pointed towards the glint spot, to collect higher signal ocean data. This strategy was updated over time, and is illustrated in Figure
22 1. The key changes were 1) the geometry of glint measurements, 2) changes to the frequency of alternating glint and nadir mode
23 orbits, 3) changes to the geometry of nadir orbits, and 4) the specification of some orbit paths as perpetual glint measurements.

24 During early instrument checkout (Aug 7, 2014), the nominal 16-day nadir/glint pattern was disrupted after very high signals were
25 observed during glint measurements. For the safety of the instrument, the observing mode was shifted to nadir measurements while
26 the cause was investigated. We concluded that an incident of glint measurements over very still water, that may have had a layer
27 of highly reflective material on its surface, was the cause of the high signal measurements (see Crisp et al. (2016b) for more
28 discussion), and they posed no risk to the instrument, so glint data collection was restarted on September 8, 2014. In mid-September
29 2014 it was recognized that the measurements were consistent with a polarization sensitivity that was rotated by 90 degrees from
30 our expectations (again, see Crisp et al. (2016b)). To improve the signal to noise of the glint mode observations, particularly near
31 the Brewster's angle, the spacecraft was yawed 30 degree during glint measurements after October 26, 2014. To provide more
32 uniform temporal distribution of glint measurements over ocean, an additional change was made to the data collection beginning
33 July 3, 2015. The nadir and glint data collection were changed to an orbit by orbit interleaving (one orbit nadir, one orbit glint, *ad*
34 *infinitum*). Over a 32-day period, nadir and glint data are collected over the same set of locations as in the original 16 day alternating
35 scheme, but the new approach does not have large time gaps in ocean data collection. In late October 2015, to reduce the
36 temperature changes of the instrument when changing from glint to nadir, the nadir geometry was updated to collect data at the
37 same 30-degree yaw as glint data are collected in. This allows for the collection of 3 to 5 glint orbits in a row between nadir orbits.
38 With this change, orbits that are solely over water, such as the Pacific and Atlantic, can be measured in glint at all times. This type

1 of data collection was started on November 12, 2015, and it is expected that this approach will be used for the remainder of the
2 mission. Figure 1 provides a calendar view of the observing strategy and data outages.

3

4 **4 Overall data flow**

5 The overall flow of the data pipeline is illustrated in Figure 2. All data products except the so called ‘Lite files’ contain one granule
6 of data, which is restricted to one mode (such as nadir, glint, target, or transition). A granule corresponds to a complete orbit of
7 measurements except in the cases where the orbit includes a switch to target measurements. In these cases there are separate data
8 product files for the target and the transition before and after the target. The data that are processed as they are collected are referred
9 to as v7, or the forward processing stream. They use calibration coefficients that are predicted based on recent measurements. This
10 dataset is created in the Science Data Operations System (SDOS) at JPL. The v7r refers to the retrospective data, or data processed
11 with calibration coefficients based on measurements before, during, and after the measurement time period. This dataset is typically
12 processed on supercomputer resources (NASA’s Pleiades and cloud computing resources).

13 The raw (L1a) measurements are geolocated, and the calibration coefficients are applied to generate geolocated, calibrated
14 radiances (L1b) as discussed in Crisp et al. (2016a). These data are then passed to the preprocessors, which are used to identify the
15 scenes that are most likely to be cloud free and successful in generating converged retrievals. One preprocessor routine also
16 provides estimates of solar induced fluorescence (SIF). The X_{CO2} retrievals are performed on a subset of data selected by the
17 preprocessors outcomes. The v7 and v7r standard (L2Std) and diagnostic (L2Dia) products report these data, which include the
18 X_{CO2} estimates. In a final step, a bias correction and data quality flag (warn level) are integrated, and each day of quality data is
19 packaged into a single so-called ‘Lite file’ (further details in Section 4.3, and in Mandrake et al., 2015). All L1B, L2 and Lite
20 products are delivered to the NASA Goddard Earth Science Data and Information Services Center (GES DISC) for distribution
21 and archiving (<http://disc.sci.gsfc.nasa.gov/OCO-2>). The L1 and L2 products are described in greater detail in the OCO-2 Data
22 Product User’s Guide and the L1B and L2 Algorithm Theoretical Basis Documents (ATBDs) and other documents, which are
23 posted along with the products at the GES DISC (<http://disc.sci.gsfc.nasa.gov/OCO-2/documentation/oco-2-v7>) (Osterman et al.,
24 2015; Crisp et al., 2014; Eldering et al., 2015; Mandrake et al., 2015).

25

26 **4.1 Calibrated radiances**

27 The “Level 1B” (L1B) product consists of full orbits or fractions of orbits of calibrated and geolocated spectral radiances from the
28 ABO2, WCO2, and SCO2 channels. The details of the transformation of raw measurements into calibrated spectral radiances are
29 discussed in the L1b Algorithm Theoretical Basis document (Eldering et al., 2015). The pre-flight spectral and radiometric
30 calibration are discussed in Lee et al. (2016) and Rosenberg et al. (2016). The in-flight performance is discussed in detail in Crisp
31 et al. (2016a). The L2 data products are not impacted by the calibration issues discussed in Crisp et al. (2016a) with the exception
32 of time dependent radiometric correction factors that are now understood to be in error for the v7/v7r data, with an increasing error
33 in time. This radiometric error has a magnitude of about 4% by 18 months into the mission, and is an error in the absolute
34 radiometry, not a growing uncertainty on the radiances. Analysis of a set of test retrievals where this error was removed showed,
35 that an absolute radiance error of 4% will impart an X_{CO2} error of 0.22 ppm, 0.12 ppm, and 0.4 ppm in nadir land, glint land, and
36 glint water measurements, respectively. This error is not addressed in the analysis presented here, where data are used as provided
37 in the v7/v7r files.

Deleted: s

Deleted: .

1

2 4.2 Preprocessors

3 For the v7 and v7r OCO-2 dataset, the A-band (ABP) (Taylor et al., 2016) and IMAP-DOAS (IDP) preprocessors (Frankenberg et
4 al., 2011, 2012, 2014) were used for the selection of data to be processed to L2. To limit the demands on the computing system,
5 no more than 6% of data collected each day are processed to L2 in the v7 forward processing stream. The v7r processing stream
6 includes all data that meets pre-processing criteria, which is on average 17.9% for glint data and 6.6% for nadir. Taylor et al (2016)
7 describes the preprocessor outcomes in detail. In summary, the A-band preprocessor compares the measured radiance spectra with
8 spectra calculated with a non-scattering forward model to test for the presence of clouds. The IDP also uses a non-scattering forward
9 model, but it is applied to the WCO2 and SCO2 bands independently. Ratios of the single band column retrievals are then analyzed
10 to identify scenes that are impacted by clouds and aerosols. As reported in Taylor et al (2016) the combined ABP and IDP OCO-2
11 preprocessors screen approximately 85-90% of the co-located data that MODIS reports to be cloudy, with overall global agreement
12 of ~85% between the two sensors. The regions of significant disagreement were found to be tropical and subtropical oceans and
13 desert land. Comparisons to CALIOP measurement of the vertical distribution of cloud optical thickness confirmed the conclusion
14 derived from simulations that the combined ABP and IDP preprocessors successfully identify high, optically thin clouds and
15 midlevel clouds and aerosols, but fail to identify contamination in about 25% of the cases of low, optically thick clouds and aerosols.
16 Additional pre-filters remove all land data south of 65S, and further limit the surface albedo in the O₂-A band to less than 0.55 for
17 a rough proxy of the presence of snow and ice on the ground, which can cause the retrievals significant problems (O'Dell et al.,
18 2012).

19

20 4.3 Level 2 algorithm products

21 The OCO-2 project reports two key products at L2 (derived geophysical data at the spatial resolution of the measurement), the dry
22 air mole fraction of carbon dioxide (X_{CO_2}) and solar induced fluorescence (SIF). As described in the preprocessor section, only a
23 subset of data are considered to be sufficiently cloud (and aerosol)-free (optical depths less than ~0.35 [as determined in the](#)
24 [preprocessors](#)) for the next step of processing in the L2 Full Physics algorithm, which produced the X_{CO_2} data product. The SIF
25 product is generated by the IDP preprocessors (Frankenberg et al., 2014). As described in Frankenberg et al., (2014), most of the
26 fluorescence signal is retained, even through moderate clouds (optical depths up to 5). As a consequence, SIF results are reported
27 for a much larger fraction of the OCO-2 observations compared to the X_{CO_2} product.

28 The OCO-2 retrievals for X_{CO_2} are created using the full physics algorithm that has been described previously (O'Dell, et al., 2012;
29 O'Dell et al., 2016). The retrieval algorithm is based on an optimal estimation scheme and an efficient radiative transfer technique
30 that accounts for multiple scattering and polarization effects. A standard cost function is minimized to find the state vector that
31 produces the maximum *a posteriori* probability. While the focus is the retrieval of X_{CO_2} , other parameters such as surface albedo,
32 aerosols, temperature, water vapor, and wind speed (for water surfaces only), are co-retrieved. Prior to the launch of OCO-2, this
33 algorithm was adapted for application to the GOSAT measurements, with these results reported in O'Dell et al. (2012) and Crisp
34 et al. (2012), and for OCO-2 it remains largely unchanged from what was reported in those papers.

35 The X_{CO_2} data are reported in the L2_Standard files and the L2_Diagnostic files, where the diagnostic files contain additional
36 information that may be useful for detailed assessment of the algorithm and for the modeling community (Osterman et al., 2015).

37 Examples of the additional information are the averaging kernels and the *a posteriori* covariance matrix, \hat{S} . In v7, the L2 Standard

1 and Diagnostic files, containing about 60,000 soundings per file, do not contain warn levels values which indicate data quality
2 (Mandrake et al., 2013), nor has a bias correction been applied. This information is calculated subsequently and included in the
3 Lite files described below.

4 A summary daily data product, referred to as the Lite files, is created, to simplify data volumes and data structures. Specific files
5 for X_{CO2} (Mandrake et al., 2015) and separately for SIF product contain one day of data per file (Frankenberg, 2015). For X_{CO2} a
6 bias correction is applied, warn levels are assigned, with all converged soundings included in the file.

7 4.3.1 L2 X_{CO2} results

8 The X_{CO2} data record from OCO-2 now extends more than 18 months, and Figures 3, 4, and 5 show maps of these X_{CO2}
9 measurements. These maps illustrate averages over month long periods, so there are nadir and glint data in each panel. The data
10 included in these maps and all that follow have been screened and have had the bias correction applied (v7rB Lite file data with
11 the 0/1 data quality flag applied, see Mandrake et al., 2015). These two processes will be discussed in more detail in Sections 4.3.4
12 and 4.3.6. As expected, these maps show the large annual changes in X_{CO2}. CO₂ builds up over the Northern Hemisphere during
13 winter, and then is rapidly removed from the atmosphere as spring arrives and the terrestrial ecosystem activity increases rapidly.
14 This is most apparent in the month of June, when the decrease of X_{CO2} over northern Asia is order 10 ppm. The overall gradients
15 of a few ppm from north to south are apparent in the data, as well as the secular increase in CO₂ from October 2014 to March 2016.
16 Other features are apparent in the data maps, such as the higher CO₂ concentrations over the Eastern US and China between October
17 and December (see Figures 3 and 5), when the overall global X_{CO2} gradient is small. Enhanced X_{CO2} coincident with biomass
18 burning in the Amazon, central Africa, and Indonesia (Van Der Werf et al., 2010) is also obvious in these figures.

Deleted: n

19 The latitudinal coverage of the v7r dataset is also apparent from these maps. Data selection for processing through L2 relies on
20 screening from the preprocessor results, as well as limitations on geographical extent. Analysis of the preprocessor data (Taylor et
21 al., 2016) show that a large fraction of these higher latitude data are marked as cloudy, which is in agreement with the MODIS
22 cloud fields. The current data selection does not select data south of 65 degrees in latitude, as experience with ACOS data showed
23 that retrievals over ice failed routinely. We intend to retrieve the small number of cloud-free scenes over bare ground at these
24 latitudes in the next version of the retrieval. Due to clouds, solar illumination and geometry, any given month has data that spans
25 about 100 degrees in latitude, but the coverage band shifts north and south with the seasons.

26 4.3.2 Signal to noise ratios

27 The OCO-2 instrument was designed to provide adequate continuum signal to noise (SNR) to achieve 0.3% precision for X_{CO2}
28 measurements. The SNR design requirements were 290, 270, and 190 at nominal radiance levels (5.8, 2.1, and 1.1 x 10¹⁹ photons
29 m⁻² sr⁻¹ μm⁻¹ s⁻¹) in the A-band, weak and strong CO₂ band, respectively. The in-flight performance has met or exceeded all
30 expectations, with SNR values as provided in the data product (radiance mean value in the continuum divided by the radiance noise
31 value in the continuum) typically between 250 and 450 for the A-band, 400 to 800 for the WCO₂ band, and 200 to 500 for the
32 SCO₂ band. Figure 6 illustrates just one month of SNR levels, as no large seasonal dependence is observed. There are spatial
33 patterns, with high SNR values over the bright deserts and in cloudy regions. The lowest SNR values are over oceans, especially
34 when observed at higher solar zenith angles, particularly for the A-band.

Formatted: Superscript

35 4.3.3 χ^2 goodness of fit parameter

36

Deleted: ▾

Formatted Table

... [1]

1
2
3
4
5
6
7
8
9
10
11
12
13
14
15
16
17
18
19
20
21
22
23
24
25
26
27
28
29
30
31
32
33
34
35

$$\chi_i^2 = \frac{\frac{1}{n} \sum (y - F(x))^2}{\frac{1}{n} \sum \epsilon^2} \quad (4.1)$$

The reduced χ^2 goodness of fit parameter is a convenient measure of the magnitude of the spectral residuals relative to the measurement error. The equation for per band (χ_i^2) is given in Equation **Error! Reference source not found.**, where where i is the band index (1..3), y is the measured radiance spectrum, ϵ is the error on the measured radiance spectrum, and $F(x)$ is the forward model with the state vector x (Crisp et al., 2014; O'Dell et al., 2012, 2016). The summation is over the n valid spectral points. As discussed in Crisp et al., 2014, the persistent spectral residuals caused by limitations in the spectroscopic input data and instrumental effects are removed by fitting to empirically derived spectral vectors. This approach systematically reduces χ^2 and also reduces the dependence of χ^2 on the signal to noise ratio.

For OCO-2, we have seen that there is little seasonal dependence, but there are clear spatial patterns, as illustrated in Figure 7. In the A-band, prominent features occur in the region of the South Atlantic Anomaly (SAA) (Crisp et al., 2016a). The effects of this region of a high density of high energy particles are seen as radiance spikes in the A-band measurements. We attempt to screen out the effects, but the fitting is still poor in this region. For the weak and strong CO₂ bands, the bright desert of the Sahara results in larger chi-square values, and mountainous regions impact the strong CO₂ fits.

4.3.4 Warn levels

The data presented in this paper have data quality screening applied. For the OCO-2 dataset, we have developed warn levels (Mandrake et al., 2013 and Mandrake et al., in prep 2016). The concept behind the warn levels is that the data are ordered by quality as defined by a number of data variance metrics, allowing the user to make decisions concerning the trade off between data volume and data quality. This is a more flexible approach than the traditional good or bad quality assignment, and reflects the fact that data quality is a continuum, not a binary quantity, and should be indicated as such. The OCO-2 warn levels range from 0 to 19, with 0 indicating the highest quality and 19 considered the lowest quality. More details of the process used to develop warn levels are reported in Mandrake et al. 2013, 2016 (in prep) as well as the OCO-2 Lite file documentation [Mandrake et al., 2015]. Our recommendation is that users should not use data above a warn level of 15 for all land data, nor above 18 for water glint. This removes approximately 25% of the land data and 10% of the water glint data.

For the v7r data, outliers were screened with a set of additional flags, related to the cloud preprocessors, aerosol optical depths, surface characteristics, etc. The detailed flagging parameters and thresholds are provided in the Lite file user's guide. The warn level thresholds and outlier screening are combined in the 0/1 flag that is included in the Lite file, to be compatible with the European Greenhouse Gas Climate Change Initiative (GHG-CCI) data product specifications (Buchwitz et al., 2015). We have used this screening for the maps shown in this paper, but strongly encourage users to carefully evaluate the warn levels that are appropriate for their science analysis.

4.3.5 Data density after quality screening

The data density after quality screening for a few select months is illustrated in Figure 8. The monthly total data density ranges from 1.3 million to 2.4 million soundings per month selected by the xco2_quality_flag in the Lite file for periods without decontamination cycles, influenced by the mixture of nadir and glint measurements, as well as clouds and season. For individual 2

Formatted: Font:Not Italic
Formatted: Font:Not Italic
Formatted: Centered

Deleted: (4-1)

Formatted: Font:Bold
Formatted: Font:Bold
Formatted: Font:Bold

1 degree by 2 degree regions, the number of soundings in a month range from a few to over a thousand. There is a roughly inverse
2 relationship, so for example, on a monthly basis, about 100 of the 2 degree by 2 degree cells have 100 soundings, and 10 have 1000
3 soundings. The preprocessors, as described in Taylor et al. (2016), limit the data that is put through L2 processing, and then
4 processing failures and data screening further trim the dataset. Nevertheless, there is a large volume of high quality data available
5 from OCO-2. The highest densities of data are over desert areas, although mid-latitude data density is high during some seasons.
6 As reported in Taylor et al. (2016) the prescreening and resulting data density is consistent with MODIS cloud statistics.

7 The cloudy region of the inter-tropical convergence zone (ITCZ) has lower data density, as does northern South America. This
8 region is impacted by clouds as well as the SAA, where cosmic ray events impact OCO-2 measurements. For the v7/v7r data, the
9 preprocessors do not account for the SAA impacts, and thus a significant fraction of data are screened out. In the next version, the
10 preprocessors will have SAA treatment integrated, and we expect that the data yield will increase in this region.

11 4.3.6 Bias correction

12 The bias correction described in O'Dell et al. (2016) and the OCO-2 documentation (Mandrake et al., 2015) was applied to the
13 X_{CO_2} data shown in Figures 3, 4, and 5. The monthly mean bias corrections for 3 sample months are shown in Figure 9. The bias
14 correction seeks to remove systematic footprint-to-footprint differences, mode-to-mode differences (for example systematic
15 differences between land glint and land nadir measurements), and systematic differences that appear to be correlated to other
16 retrieval variables. Two predictive variables are currently used in the bias correction for land retrievals, and three are used for ocean
17 retrievals. In addition, the bias correction process puts the OCO-2 data on the same scale as the Total Carbon Column Observing
18 Network (TCCON) ground-based measurements, which are tied to the WMO scale for carbon dioxide (Wunch et al., 2016, 2010,
19 2011). The OCO-2 mission development included a validation plan which recognized the need for the TCCON network and a
20 special data collection mode to gather adequate validation data. A detailed discussion of the ground-based data and the OCO-2 data
21 that are collected in target mode at these locations can be found in Wunch et al., 2016. Details of the derivation of the bias correction
22 and its relationship to other variables can be found in O'Dell et al. (2016). The monthly distribution of the bias correction values
23 are well described by Gaussian distributions. Overall, for the water glint observations on monthly scales, the mean of the
24 distribution is 0.0 to 0.4 ppm, with a standard deviation of about 0.55ppm. For land glint observations, the mean is larger, 0.9 to
25 1.1 ppm, and the standard deviation is typically 1.2 ppm. The land nadir distribution has a similar standard deviation, about 1.2ppm,
26 with a mean of 1.3 to 1.8 ppm. The patterns strongly follow latitudinal gradients, likely driven by viewing geometry with aerosol
27 and cloud scattering becoming more important as the instrument views through longer paths of the atmosphere. The bias correction
28 is described in more detail in O'Dell et al. (2016).

29

30 4.3.7 Uncertainty on X_{CO_2} product

31 The OCO-2 data products include an estimate of the uncertainty on the X_{CO_2} data. As discussed by Connor et al. (2008, 2016), this
32 estimate is a lower bound, as it includes error related to the noise on the radiance measurement, the smoothing error, and
33 interference error. Propagation of systematic errors in input terms for the forward model to the X_{CO_2} estimate is not considered in
34 the error estimate reported in the v7/v7r L2 products. Figure 10 is a set of maps of the average X_{CO_2} uncertainty from the data
35 product for a six-month period. This shows that the estimated uncertainty is generally smaller over water than the land surface and
36 that the uncertainty is larger at the extreme latitudes, where interference errors grow. Worden et al. (2016) have made a careful
37 assessment of the OCO-2 uncertainty estimates, by evaluating the standard deviation of the difference from the mean X_{CO_2} for
38 collections of soundings within 100km in latitude. They compare this to the expected standard deviation due to noise. This research

1 showed that while linearly correlated, the X_{CO_2} calculated measurements error in the data product appears to underestimate the
2 empirically-derived X_{CO_2} measurement error by a factor of approximately 2, with a larger underestimate for land data and a smaller
3 underestimate for water glint measurements.

4 In the optimal estimation retrieval, algorithm input choices such as the *a priori* mean state vector (\mathbf{x}_a) and *a priori* covariance (\mathbf{S}_a),
5 or constraint, can impact the variability in the retrieval error in X_{CO_2} . The *a posteriori* covariance matrix ($\hat{\mathbf{S}}$) is also an important
6 output of the L2 retrieval process, as it is critical for the data assimilation process used to determine CO_2 fluxes. The OCO-2 project
7 is in the midst of an evaluation of this quantity and the accuracy of the algorithm's reported uncertainty as a measure of the error
8 variability, through the use of large-scale simulations. By running simplified retrievals over large ensembles of input variables
9 (priors, constraints, and other parameters), one can assess the characteristics of the retrieval bias and variance and evaluate what is
10 reported in the data product (Hobbs et al., 2016). The choice of prior becomes particularly impactful for moderate to large aerosol
11 optical depths (0.1 or more).

12 There are many other variables that are co-retrieved with the X_{CO_2} , including surface pressure, aerosol optical depth, surface albedo,
13 water profile scaling factor, and an offset of the temperature profile. The aerosol optical depths are being compared against
14 independent measurements, such as AERONET optical depths while an analysis of the retrieved water vapor profiles against
15 SuomiNet and the Advanced Microwave Scanning Radiometer-2 (AMSR-2) is also being conducted (Nelson and O'Dell, 2016).
16 As discussed in detail in O'Dell et al. (2016), many of these parameters will compensate for one another in the retrieval algorithm,
17 so must be considered 'effective quantities' (e.g. 'effective albedo' and 'effective optical depth') as they are the values that
18 minimize the fit in an optimal estimation scheme, but they are at times not directly related to the physical quantity (Kulawik et al.,
19 2006, Eldering et al., 2008). The performance and relationships of these parameters are discussed at length in O'Dell et al., 2016.

20 **4.4 Solar induced fluorescence**

21 Using GOSAT and GOME-2 spectra, Frankenberg et al. (2011, 2012, 2014, 2015; Joiner et al. 2011) demonstrated that using the
22 observed Fraunhofer line fractional depths, solar-induced fluorescence of chlorophyll can be quantified. Frankenberg et al. (2014)
23 performed a pre-flight assessment of the fluorescence measurement performance of OCO-2. This measurement approach is being
24 applied to the OCO-2 data, motivated in part because neglect of this phenomenon results in errors in surface pressure and aerosol
25 optical depth, which propagate into a small bias in the X_{CO_2} retrieval (Frankenberg et al., 2012).

26 The IDP preprocessor performs the SIF retrieval, along with single band retrievals of the water and CO_2 columns that are used for
27 cloud screening purposes. As described in Frankenberg et al. (2014) the SIF retrieval is impacted less strongly by clouds than the
28 X_{CO_2} retrieval, so useful data is collected over a much larger number of soundings. However, high single-measurement precision
29 errors warrant aggregation in space and/or time for scientific use. The SIF product is derived at two wavelengths, 757nm and
30 771nm, and it is recommended that the user examine both fields independently, as this first dataset (v7r) may have different errors
31 in each product.

32 Figures 11 illustrates a year of SIF retrievals, where data has been averaged across seasons. These show expected features, such as
33 the high SIF values in the regions of intense agriculture during early summer, and the low SIF in the Northern Hemisphere during
34 its winter. The SIF signal in the tropics has some seasonality to it, but is always larger than $0.5 \text{ W m}^2 \mu\text{m}^{-1} \text{ sr}^{-1}$.

35 Campaigns are underway to compare OCO-2 measurements to data at flux towers and to underfly the OCO-2 measurements with
36 an aircraft-mounted grating spectrometers. Details of these inter-comparisons are in Sun et al. (in prep, 2016). The objective of
37 those studies is to quantify the relationship of OCO-2 derived SIF with independent measurements.

1
2
3
4
5
6
7
8
9
10
11
12
13
14
15
16
17
18
19
20
21
22
23
24
25
26
27
28
29
30
31
32
33
34

5 Gradients and trends in observed X_{CO2}

5.1 Growth rate of X_{CO2}

The dense, global dataset from OCO-2 can be used to assess the annual growth rate of X_{CO2}. Figure 12 shows the annual zonal growth rates derived from OCO-2 for 5 different 12 month periods. The growth rate as determined from the NOAA ESRL station at Mauna Loa is shown for comparison. The growth rates are generally between 2.5 and 3 ppm per 12 months from 2014 to 2015, which includes the largest growth rate ever recorded at the Mauna Loa Observatory. More detailed analysis of the growth rate such as that presented for GOSAT data in Kulawik et al. (2016) and Lingqvist et al. (2015) are required to quantitatively assess the growth rate from OCO-2, but this first look shows the OCO-2 has a reasonable range of values. The figure also illustrates the longitudinal standard deviation of the OCO-2 data for each latitude band. Note that the Mauna Loa Observatory is a background site, whereas the OCO-2 measurements span both background sites and populated regions. This variability may drive the standard deviation, although OCO-2 glint retrievals over water tend to have lower variability than OCO-2 land retrievals, which could also explain the standard deviation. The relative sampling of regions of emissions and uptake differs in time with OCO-2, which will result in a different 12-month growth rate than that derived from the NOAA ESRL station.

5.2 Seasonal cycle of X_{CO2} near Hawaii

A time series of weekly average X_{CO2} from OCO-2 for a region around Hawaii is shown in Figure 13. For this analysis, we have selected glint data over water only, applied the quality flag, and gathered data from a region that span from 175° W to 130° W in longitude, and from 15° N to 25° N in latitude. The time series clearly shows weekly and monthly changes as observed by OCO-2. The standard deviation of the weekly-averaged data range from 0.5 to 0.8 ppm, smaller than the seasonal changes and at times the monthly changes. There are 2000 to 20,000 measurements averaged per week for the OCO-2 data. The timeseries shows little growth between January and February 2015, and in early 2016. The minimum of the year occurs in August and September, similar to the timing of the minimum in surface measurements. Now that OCO-2 has a full two year record, seasonal cycle analysis such as that in Lingqvist et al. (2015) can be conducted with OCO-2 data. Wunch et al. (2016) provide timeseries at all of the TCCON locations, with all OCO-2 measurement mode data (nadir, glint, target).

5.3 Assessment of overall data quality

The OCO-2 mission has been successful in collecting over a million measurements of radiance spectra in the A-band, weak and strong CO₂ bands each day. After screening for clouds, and applying post retrieval quality flags, OCO-2 typically delivers 100,000 global measurements of CO₂ per day. Detailed comparisons have been made against the Total Column Carbon Observing Network, and the OCO-2 measurements agree within 1 ppm in most cases (see Wunch et al., 2016).

There are regions of the world that have consistent high data yields, such as desert regions and the oceans to the north and south of the cloudy ITCZ. Regions of persistently low data yield include the region over South America that is impacted by the South

Deleted: ,
Deleted: and t
Deleted: s

Deleted: water

Deleted: The ground-based measurements collected at Mauna Loa Observatory are overplotted, although OCO-2 data are not directly comparable to the NOAA ESRL and other ground-based measurements, because OCO-2 senses the total column of X_{CO2} rather than surface concentrations. If the vertical gradient of CO₂ is small, we expect similar values for the two measurements, whereas the surface measurements will be larger than the OCO-2 X_{CO2} measurements if there are CO₂ enhancements in the lower atmosphere.

Deleted: Both datasets

Deleted: The surface measurements and X_{CO2} are most similar

Deleted: and the X_{CO2} further north is nearly the same as Mauna Loa surface CO₂ concentrations in August through October. The differences between the total column and surface measurements are greatest in the early spring, as the build-up of CO₂ in the Northern Hemisphere is present in the near surface layers, but has not propagated vertically to the X_{CO2} signal. The standard deviation of the weekly-averaged data range from 0.5 to 0.8 ppm, with 2000 to 20,000 measurements averaged per week for the OCO-2 data

Deleted: .

Formatted: English (US)

Deleted: <#>Latitudinal gradient [2]

1 Atlantic Anomaly, ocean regions of the ITCZ, and regions where the solar zenith angles are large (especially northern latitudes in
2 NH winter, and southern latitudes during SH winter).

3 The dataset is consistent in time, showing stability in diagnostic parameters such as the measurement SNR and retrieval χ^2 as well
4 as the overall data density. Not surprisingly, there are some data features that are inconsistent with the validation dataset, and
5 different from model predictions. The largest feature is a high bias in X_{CO_2} over water for southern latitudes during the Southern
6 Hemisphere winter. This issue is apparent in the TCCON comparisons for Wollongong shown in Wunch et al. (2016), and in the
7 comparison to models presented in O'Dell et al. (2016). This bias has been extensively examined by the OCO-2 teams, who have
8 considered viewing geometry, polarization effects, interferences such as aerosols, surface models, and instrument performance. The
9 analysis has not yet yielded insights into the root cause, although in early testing, there are indications that the lack of stratospheric
10 aerosols in the current version of the retrieval algorithm can significantly increase bias.

11 The v7/v7r data version discussed here is the current operational data product. In the future, a v8/v8r data product will be produced
12 that addresses calibration issues as described in Crisp et al. (2016ab), as well as retrieval algorithm improvements described in
13 O'Dell et al. (2016) such as the land surface treatment and others that are not yet fully tested. Future changes to the retrieval
14 algorithm will focus on improving the parameterization of the patterns of bias for correction, if not direct reduction of the bias.

15

16 **6 Conclusions**

17 The OCO-2 mission has been successful in collecting a dense, global set of high-spectral resolution measurements that are used to
18 estimate the column-averaged atmospheric CO_2 dry air mole fraction, X_{CO_2} . The first 18 months of the mission have provided 1.3
19 to 2.4 million X_{CO_2} measurements per month after screening for data quality. As described in Wunch et al. (2016), the data have
20 median difference of less than 0.5 ppm with the primary ground-based validation network, and RMS differences typically below
21 1.5 ppm. This statistic from Wunch et al. (2016) is for data with a warn level below 11 and an “outcome flag” of zero, which are
22 slightly less strict selection criteria than the 0/1 quality flag. Large-scale features, such as the drawdown of CO_2 in the Northern
23 Hemisphere spring and the increase of CO_2 over Northern Hemisphere winter are obvious in the data. By meeting the mission goals
24 for accuracy, resolution, and coverage, the OCO-2 mission has provided a dataset that can now be used to assess regional-scale
25 sources (emitters) and sinks (absorbers) around the globe.

26

27 **7 Data Availability**

28 All of the OCO-2 data products are publically available through the NASA Goddard Earth Science Data and Information Services
29 Center (GES DISC) for distribution and archiving (<http://disc.sci.gsfc.nasa.gov/OCO-2>).

30

31 **Acknowledgements**

32 Part of this work was conducted at the Jet Propulsion Laboratory, California Institute of Technology under contract with the
33 National Aeronautics and Space Administration (NASA) for the Orbiting Carbon Observatory-2 Project. Work at Colorado State
34 University and The Geology and Planetary Sciences Department at the California Institute of Technology were supported by
35 subcontracts from the OCO-2 Project. The NOAA ESRL ground-based weekly averaged measurements from Mauna Loa
36 Observatory were obtained from www.esrl.noaa.gov/gmd/ccgg/trends/.

37

1 **References**

2

3 Arora, V.K., Boer, G.J., Friedlingstein, P., Eby, M., Jones, C.D., Christian, J.R., Bonan, G., Bopp, L., Brovkin, V., Cadule, P. and
4 Hajima, T.: Carbon–concentration and carbon–climate feedbacks in CMIP5 Earth system models, *Journal of Climate*, 26, 5289-
5 5314, 2013.

6 Basilio, R. R., Pollock, H., and Hunyadi-Lay, S.L.: OCO-2 (Orbiting Carbon Observatory-2) mission operations planning and
7 initial operations experiences. SPIE Remote Sensing, International Society for Optics and Photonics, 2014.

8 Bösch, H., Toon, G., Sen, B., Washenfelder, R., Wennberg, P., Buchwitz, M., de Beek, R., Burrows, J., Crisp, D., Christi, M.,
9 Connor, B. J., Natraj, V., and Yung, Y. L.: Space-based near-infrared CO₂ measurements: Testing the Orbiting Carbon Observatory
10 retrieval algorithm and validation concept using SCIAMACHY observations over Park Falls, Wisconsin, *J. Geophys. Res.*, 111,
11 0148–0227, doi: 10.1029/2006JD007080, 2006.

12 Bösch, H., Baker, D., Connor, B., Crisp, D., and Miller, C.: Global characterization of CO₂ column retrievals from shortwave-
13 infrared satellite observations of the Orbiting Carbon Observatory-2 Mission, *Remote Sensing*, 3, 270–304,
14 doi:10.3390/rs3020270, 2011.

15 Buchwitz, M., de Beek, R., Noel, S., Burrows, J. P., Bovensmann, H., Schneising, O., Khlystova, I., Bruns, M., Bremer, H.,
16 Bergamaschi, P., Körner, S., and Heimann, M.: Atmospheric carbon gases retrieved from SCIAMACHY by WFM-DOAS: version
17 0.5 CO and CH₄ and impact of calibration improvements on CO₂ retrieval, *Atmos. Chem. Phys.*, 6, 2727–2751, doi:10.5194/acp-
18 6-2727-2006, 2006.

19 ~~Buchwitz, M., Reuter, M., Schneising, O., Boesch, H., Guerlet, S., Dils, B., Aben, I., Armante, R., Bergamaschi, P., Blumenstock,~~
20 ~~T. and Bovensmann, H.: The Greenhouse Gas Climate Change Initiative (GHG-CCI): Comparison and quality assessment of near-~~
21 ~~surface-sensitive satellite-derived CO₂ and CH₄ global data sets, *Remote Sensing of Environment*, 162, pp.344-362, 2015.~~

22 Burrows J. P., Hölzle, E., Goede, A. P. H., Visser, H. and Fricke, W.: SCIAMACHY - Scanning Imaging Absorption Spectrometer
23 for Atmospheric Chartography. *Acta Astronautica*, 35, 445-451, 1995.

24 Chevallier, F., Palmer, P.I., Feng, L., Bösch, H., O'Dell, C.W. and Bousquet, P.: Toward robust and consistent regional CO₂ flux
25 estimates from in situ and spaceborne measurements of atmospheric CO₂, *Geophys. Res. Lett.*, 41, 1065–1070, doi:10.1002/
26 2013GL058772, 2014.

27 Connor, B. J., Bösch, H., Toon, G., Sen, B., Miller, C., and Crisp, D.: Orbiting Carbon Observatory: Inverse method and prospective
28 error analysis, *J. Geophys. Res.*, 113, D05305, doi:10.1029/2006JD008336, 2008.

29 Connor, B., Bösch, H., McDuffie, J., Taylor, T., Fu, D., Frankenberg, C., O'Dell, C., H. Payne, V.H., Gunson, M.R., Pollock, H.,
30 Hobbs, J., Oyafuso, F., and Jiang, Y.: Quantification of uncertainties in OCO-2 measurements of X_{CO2}: simulations and linear error
31 analysis, *Atmospheric Measurement Techniques*, in review, 2016

32 Crisp, D., Atlas, R.M., Breon, F.-B., Brown, L.R., Burrows, J.P., Ciais, P., Connor, B.J., Doney, S.C., Fung, I.Y., Jacob, D.J.,
33 Miller, C.E., O'Brien, D., Pawson, S., Randerson, J.T., Rayner, P., Salawitch, R.J., Sander, S.P., Sen, B., Stephens, G.L., Tans,
34 P.P., Toon, G.C., Wennberg, P.O., Wofsy, S.C., Yung, Y.L., Kuang, Z., Chudasama, B., Sprague, G., Weiss, B., Pollock, R.,
35 Kenyon, D., Schroll, S.: The Orbiting Carbon Observatory (OCO) mission, *Advances in Space Research*, 34, 700–709, 2004.

Deleted: Buchwitz, Michael, et al.: The Greenhouse Gas Climate Change Initiative (GHG-CCI): Comparison and quality assessment of near-surface-sensitive satellite-derived CO₂ and CH₄ global data sets, *Remote Sensing of Environment*, 162, 344-362, 2015.

Formatted: Font:Not Italic

Formatted: Font:Not Italic

Formatted: English (US)

1 Crisp, D., Miller, C.E., DeCola, P.L.: NASA Orbiting Carbon Observatory: measuring the column averaged carbon dioxide mole
2 fraction from space, *J. Appl. Remote Sens.*, 2, 023508; doi:10.1117/1.2898457., 2008.

3 Crisp, D., Fisher, B. M., O'Dell, C., Frankenberg, C., Basilio, R., Bösch, H., Brown, L. R., Castano, R., Connor, B., Deutscher,
4 N.M., Eldering, A., Griffith, D., Gunson, M., Kuze, A., Mandrake, L., McDuffie, J., Messerschmidt, J., Miller, C. E., Morino, I.,
5 Natraj, V., Notholt, J., O'Brien, D.M., Oyafuso, F., Polonsky, I., Robinson, J., Salawitch, R., Sherlock, V., Smyth, M., Suto, H.,
6 Taylor, T. E., Thompson, D. R., Wennberg, P. O., Wunch, D., and Yung Y. L.: The ACOS CO₂ retrieval algorithm--Part II: Global
7 X_{CO₂} data characterization, *Atmos. Meas. Tech.*, 5, 687–707, 2012.

8 Crisp et al., Orbiting Carbon Observatory (OCO) – 2 Level 2 Full Physics Algorithm Theoretical Basis Document, Tech. Rep. D-
9 55207, NASA Jet Propulsion Laboratory, California Institute of Technology, Version 2.0, Rev 2,
10 http://disc.sci.gsfc.nasa.gov/OCO-2/documentation/oco-2-v5/OCO-2_ATBD_140530_with_ASF.pdf (last access June, 2016),
11 2014.

12 [Crisp, D., Pollock, H. R., Rosenberg, R., Chapsky, L., Lee, R. A. M., Oyafuso, F. A., Frankenberg, C., O'Dell, C. W., Bruegge, C.](#)
13 [J., Doran, G. B., Eldering, A., Fisher, B. M., Fu, D., Gunson, M. R., Mandrake, L., Osterman, G. B., Schwandner, F. M., Sun, K.,](#)
14 [Taylor, T. E., Wennberg, P. O., and Wunch, D.: The On-Orbit Performance of the Orbiting Carbon Observatory-2 \(OCO-2\)](#)
15 [Instrument and its Radiometrically Calibrated Products, *Atmos. Meas. Tech. Discuss.*, doi:10.5194/amt-2016-281, in review, 2016.](#)

16 Crisp et al., Evolution of the Orbiting Carbon Observatory-2 (OCO-2) observing strategy, in preparation, 2016b.

17 Dlugokencky, E. and Tans, P.: Trends in atmospheric carbon dioxide, National Oceanic & Atmospheric Administration, Earth
18 System Research Laboratory (NOAA/ESRL), available at: <http://www.esrl.noaa.gov/gmd/ccgg/trends>, last access: 7 October 2015.

19 Eldering, A., Kulawik, S.S., Worden, J., Bowman, K., and Osterman, G.: Implementation of cloud retrievals for TES atmospheric
20 retrievals: 2. Characterization of cloud top pressure and effective optical depth retrievals, *J. Geophys. Res.*, 113, D16S37,
21 doi:10.1029/2007JD008858., 2008.

22 Eldering, A., Pollock, R., Lee, R., Rosenberg, R., Oyafuso, F., Crisp, D., Granat, R.: Orbiting Carbon Observatory (OCO) – 2 Level
23 1B Theoretical Basis Document, Tech. Rep. D-55206, NASA Jet Propulsion Laboratory, California Institute of Technology,
24 Version 1.2, Rev 1, http://disc.sci.gsfc.nasa.gov/OCO-2/documentation/oco-2-v7/OCO2_L1B_ATBD.V7.pdf, (last access June
25 2016), 2015.

26 Feng, L., Palmer, P. I., Parker, R. J., Deutscher, N. M., Feist, D. G., Kivi, R., Morino, I., and Sussmann, R.: Estimates of European
27 uptake of CO₂ inferred from GOSAT X_{CO₂} retrievals: sensitivity to measurement bias inside and outside Europe, *Atmos. Chem.*
28 *Phys.*, 16(3), 1289–1302, doi:10.5194/acp-16-1289-2016, 2016.

29 Frankenberg, C.: Solar Induced Chlorophyll Fluorescence OCO-2 lite files (B7000) user guide, Technical Report, NASA Jet
30 Propulsion Laboratory, California Institute of Technology, [http://disc.sci.gsfc.nasa.gov/OCO-2/documentation/oco-2-](http://disc.sci.gsfc.nasa.gov/OCO-2/documentation/oco-2-v7/OCO2_SIF_B7000_Product_Description_090215.pdf)
31 [v7/OCO2_SIF_B7000_Product_Description_090215.pdf](http://disc.sci.gsfc.nasa.gov/OCO-2/documentation/oco-2-v7/OCO2_SIF_B7000_Product_Description_090215.pdf), (last access July 2016), 2015.

32 Frankenberg, C., Butz, A., and Toon, G. C.: Disentangling chlorophyll fluorescence from atmospheric scattering effects in O₂ A-
33 band spectra of reflected sun-light, *Geophysical Research Letters*, 38(3), 2011.

34 Frankenberg, C., O'Dell, C., Guanter, L., & McDuffie, J.: Remote sensing of near-infrared chlorophyll fluorescence from space in
35 scattering atmospheres: implications for its retrieval and interferences with atmospheric CO₂ retrievals, *Atmospheric Measurement*
36 *Techniques*, 5(8), 2081-2094, 2012.

Deleted: Crisp et al. ; The on-orbit performance of the Orbiting Carbon Observatory-2 (OCO-2) instrument, in preparation, 2016a. .

- 1 Frankenberg, C., O'Dell, C., Berry, J., Guanter, L., Joiner, J., Köhler, P., Pollock, R., and Taylor, T. E.: Prospects for chlorophyll
2 fluorescence remote sensing from the Orbiting Carbon Observatory-2, *Remote Sensing of Environment*, 147, 1-12, 2014.
- 3 Friedlingstein, P., Cox, P., Betts, R., Bopp, L., Von Bloh, W., Brovkin, V., Cadule, P., Doney, S., Eby, M., Fung, I. and Bala, G.:
4 Climate-carbon cycle feedback analysis: Results from the C4MIP model intercomparison, *Journal of Climate*, 19(14), 3337-3353,
5 2006.
- 6 Guerlet, S., Basu, S., Butz, A., Krol, M., Hahne, P., Houweling, S., Hasekamp, O. P., and Aben, I.: Reduced carbon uptake during
7 the 2010 Northern Hemisphere summer from GOSAT, *Geophys. Res. Lett.*, 40, 2378–2383, doi:10.1002/grl.50402, 2013.
- 8 Hobbs, J., Braverman, A., Cressie, N., Granat, R., and Gunson, M.: Uncertainty quantification for remote sensing retrievals. Under
9 review, 2016.
- 10 Joiner, J., Yoshida, Y., Vasilkov, A.P. and Middleton, E.M.: First observations of global and seasonal terrestrial chlorophyll
11 fluorescence from space, *Biogeosciences* 8.3, 637-651, 2011.
- 12 Kulawik, S. S., Worden, J., Eldering, A., Bowman, K., Gunson, M., Osterman, G. B., Zhang, L., Clough, S., Shephard, M. W.,
13 and Beer, R.: Implementation of cloud retrievals for Tropospheric Emission Spectrometer (TES) atmospheric retrievals: part 1.
14 Description and characterization of errors on trace gas retrievals, *J. Geophys. Res.*, 111, D24204, doi:10.1029/2005JD006733,
15 2006.
- 16 Kulawik, S., Wunch, D., O'Dell, C., Frankenberg, C., Reuter, M., Oda, T., Chevallier, F., Sherlock, V., Buchwitz, M., Osterman,
17 G., Miller, C. E., Wennberg, P. O., Griffith, D., Morino, I., Dubey, M. K., Deutscher, N. M., Notholt, J., Hase, F., Warneke, T.,
18 Sussmann, R., Robinson, J., Strong, K., Schneider, M., De Mazière, M., Shiomi, K., Feist, D. G., Iraci, L. T., and Wolf, J.:
19 Consistent evaluation of ACOS-GOSAT, BESD-SCIAMACHY, CarbonTracker, and MACC through comparisons to TCCON,
20 Atmos. Meas. Tech., 9, 683-709, doi:10.5194/amt-9-683-2016, 2016.
- 21 Le Quéré, C., Moriarty, R., Andrew, R. M., Canadell, J. G., Sitch, S., Korsbakken, J. I., Friedlingstein, P., Peters, G. P., Andres,
22 R. J., Boden, T. A., Houghton, R. A., House, J. I., Keeling, R. F., Tans, P., Armeth, A., Bakker, D. C. E., Barbero, L., Bopp, L.,
23 Chang, J., Chevallier, F., Chini, L. P., Ciais, P., Fader, M., Feely, R. A., Gkritzalis, T., Harris, I., Hauck, J., Ilyina, T., Jain, A. K.,
24 Kato, E., Kitidis, V., Klein Goldewijk, K., Koven, C., Landschützer, P., Lauvset, S. K., Lefèvre, N., Lenton, A., Lima, I. D., Metzl,
25 N., Millero, F., Munro, D. R., Murata, A., Nabel, J. E. M. S., Nakaoka, S., Nojiri, Y., O'Brien, K., Olsen, A., Ono, T., Pérez, F. F.,
26 Pfeil, B., Pierrot, D., Poulter, B., Rehder, G., Rödenbeck, C., Saito, S., Schuster, U., Schwinger, J., Séférian, R., Steinhoff, T.,
27 Stocker, B. D., Sutton, A. J., Takahashi, T., Tilbrook, B., van der Laan-Luijkx, I. T., van der Werf, G. R., van Heuven, S.,
28 Vandemark, D., Viovy, N., Wiltshire, A., Zaehle, S., and Zeng, N.: Global carbon budget 2015, *Earth Syst. Sci. Data*, 7, 349-396,
29 doi:10.5194/essd-7-349-2015, 2015.
- 30 Lee, R.A.M., O'Dell, C.W., Wunch, D., Roehl, C., Osterman, G.B., Blavier, J.F., Rosenberg, R., Chapsky, L., Frankenberg, C.,
31 Hunyadi-Lay, S.L. and Fisher, B.M.: Preflight spectral calibration of the Orbiting Carbon Observatory 2, *IEEE T. Geosci. Remote*,
32 submitted, 2016
- 33 Lindqvist, H., O'Dell, C. W., Basu, S., Boesch, H., Chevallier, F., Deutscher, N., Feng, L., Fisher, B., Hase, F., Inoue, M., Kivi,
34 R., Morino, I., Palmer, P. I., Parker, R., Schneider, M., Sussmann, R., and Yoshida, Y.: Does GOSAT capture the true seasonal
35 cycle of carbon dioxide?. *Atmos. Chem. Phys.*, 15, 13023-13040, doi:10.5194/acp-15-13023-2015, 2015.
- 36 Mandrake, L., Frankenberg, C., O'Dell, C. W., Osterman, G., Wennberg, P., and Wunch, D.: Semi-autonomous sounding selection
37 for OCO-2, *Atmospheric Measurement Techniques Discussions*, 6(3), 5881-5922, 2013.

Deleted: ... &

Deleted: et al

Formatted: English (US)

Formatted: English (US)

1 Mandrake, L., O'Dell, C., Wunch, D., Wennberg, P.O., Fisher, B., Osterman, G.B., Eldering, A.: Lite Files, Warn Levels, and Bias
2 Correction Determination, NASA Jet Propulsion Laboratory, California Institute of Technology, Version 1,
3 http://disc.sci.gsfc.nasa.gov/OCO-2/documentation/oco-2-v7/OCO2_XCO2_Lite_Files_and_Bias_Correction_0915_sm.pdf (last
4 access July 2016), 2015.

5 Mandrake et al.; OCO-2's quality estimation and data filtering product: A complete description of the DOGO warn levels from
6 construction to function, in [preparation](#), 2016

7 Miller, C.E., Crisp, D., DeCola, P.L., Olsen, S.C., Randerson, J.T., Michalak, A.M., Alkhaled, A., Rayner, P., Jacob, D.J.,
8 Suntharalingam, P. and Jones, D.B.A.: Precision requirements for space-based X_{CO2} data, Journal of Geophysical Research:
9 Atmospheres, 112(D10), 2007.

10 Nakajima, M., Kuze, A., Kawakami, S., Shiomi, K., and Suto, H.: Monitoring of the greenhouse gases from space by GOSAT.,
11 International Archives of the Photogrammetry, Remote Sensing and Spatial Information Science, XXXVIII, Part 8, JAXA Special
12 Session-5, 2010.

13 ~~Nelson, R. R., Crisp, D., Ott, L.E., and O'Dell, C.W.: High-accuracy measurements of total column water vapor from the Orbiting~~
14 ~~Carbon Observatory-2, Geophysical Research Letters, 2016.~~

15 ~~O'Dell, C. W., Connor, B., Bösch, H., O'Brien, D., Frankenberg, C., Castano, R., Christi, M., Crisp, D., Eldering, A., Fisher, B.,~~
16 ~~Gunson, M., McDuffie, J., Miller, C. E., Natraj, V., Oyafuso, F., Polonsky, I., Smyth, M., Taylor, T., Toon, G. C., Wennberg, P. O.,~~
17 ~~and Wunch, D.: The ACOS CO₂ retrieval algorithm – Part 1: Description and validation against synthetic observations, Atmos.~~
18 ~~Meas. Tech., 5, 99-121, 2012.~~

19 ~~O'Dell et al.; The OCO-2 v7 X_{CO2} retrieval algorithm: description and performance evaluation, in preparation, 2016.~~

20 Osterman, G.B., Eldering, A., Avis, C., O'Dell, C.W, Martinez, E., Crisp, D., Frankenberg, C., Fisher, B.: ACOS Level 2 Standard
21 Product Data User's Guide, v3.5, Revision D, [http://disc.sci.gsfc.nasa.gov/OCO-2/documentation/gosat-acos/gosat-](http://disc.sci.gsfc.nasa.gov/OCO-2/documentation/gosat-acos/gosat-acosdoc/ACOS_v3.5_DataUsersGuide.pdf)
22 [acosdoc/ACOS_v3.5_DataUsersGuide.pdf](http://disc.sci.gsfc.nasa.gov/OCO-2/documentation/gosat-acos/gosat-acosdoc/ACOS_v3.5_DataUsersGuide.pdf), (last access July 2016), 2016.

23 Rayner, P. J., and O'Brien, D. M.: The utility of remotely sensed CO₂ concentration data in surface source inversions, Geophysical
24 Research Letters, 28(1), 175-178, 2001.

25 Rosenberg, R., Maxwell, S., Johnson, B.C., Chapsky, L., Lee, R.A.M., Pollock, H.R.: Preflight radiometric calibration of Orbiting
26 Carbon Observatory 2, IEEE Transaction on Geoscience and Remote Sensing (TGRS), in review, 2016.

27 Reuter, M., Buchwitz, M., Hilker, M., Heymann, J., Schneising, O., Pillai, D., Bovensmann, H., Burrows, J. P., Bösch, H., Parker,
28 R., Butz, A., Hasekamp, O., O'Dell, C. W., Yoshida, Y., Gerbig, C., Nehrkorn, T., Deutscher, N. M., Warneke, T., Notholt, J.,
29 Hase, F., Kivi, R., Sussmann, R., Machida, T., Matsueda, H., and Sawa, Y.: Satellite-inferred European carbon sink larger than
30 expected, Atmos. Chem. Phys., 14, 13739-13753, doi:10.5194/acp-14-13739-2014, 2014.

31 Schimel, D., Stephens, B.B., and Fisher, J.B.: Effect of increasing CO₂ on the terrestrial carbon cycle, PNAS, 112, 436-441., doi:
32 10.1073/pnas.1407302112, 2015.

33 ~~Schneising, O., Reuter, M., Buchwitz, M., Heymann, J., Bovensmann, H., and Burrows, J. P.: Terrestrial carbon sink observed~~
34 ~~from space: variation of growth rates and seasonal cycle amplitudes in response to interannual surface temperature variability,~~
35 ~~Atmospheric Chemistry and Physics, 14(1), 133-141, doi:10.5194/acp-14-133-2014, 2014.~~

Formatted: Font:Not Italic

Deleted: Nelson, R., and O'Dell, C.W.: Total column water vapor from OCO-2, in preparation, 2016. .

Deleted: i

Deleted: &

1 Sun, Y., et al., Solar-induced chlorophyll fluorescence from the Orbiting Carbon Observatory-2 (OCO-2): The spatial-temporal
2 patterns and relationships with gross primary productivity (in prep), 2016.

3 Takahashi, T., Sutherland, S.C., Wanninkhof, R., Sweeney, C., Feely, R.A., Chipman, D.W., Hales, B., Friederich, G., Chavez, F.,
4 Sabine, C. and Watson, A.: Climatological mean and decadal change in surface ocean pCO₂, and net sea-air CO₂ flux over the
5 global oceans. Deep Sea Research Part II: Topical Studies in Oceanography, 56(8), 554-577, 2009.

6 Taylor, T.E., O'Dell, C.W., Partain, P.T., Cronk, H.Q., Nelson, R.R., Rosenthal, E.J., Chang, A.Y., Osterman, G.B., Pollock, R.H.
7 and Gunson, M.R.: Orbiting Carbon Observatory-2 (OCO-2) cloud screening algorithms: validation against collocated MODIS
8 and CALIOP data, Atmospheric Measurement Techniques, 9(3), 973, 2016.

9 Van der Werf, G.R., Randerson, J.T., Giglio, L., Collatz, G.J., Mu, M., Kasibhatla, P.S., Morton, D.C., DeFries, R.S., Jin, Y.V.
10 and van Leeuwen, T.T.: Global fire emissions and the contribution of deforestation, savanna, forest, agricultural, and peat fires
11 (1997–2009). Atmospheric Chemistry and Physics, 10(23), pp.11707-11735, 2010.

12 Worden, J., Doran, G., Kulawik, S.S., Eldering, A., Crisp, D., Frankenberg, C., O'Dell, C., and Bowman, K.: Evaluation,
13 validation, and attribution of OCO-2 X_{CO2} uncertainties, in review, 2016.

14 Wunch, D., Toon, G.C., Wennberg, P.O., Wofsy, S.C., Stephens, B.B., Fischer, M.L., Uchino, O., Abshire, J.B., Bernath, P., Biraud,
15 S.C. and Blavier, J.F.: Calibration of the Total Carbon Column Observing Network using aircraft profile data, Atmospheric
16 Measurement Techniques, 3(5), 1351-1362, 2010.

17 Wunch, D., Wennberg, P.O., Toon, G.C., Connor, B.J., Fisher, B., Osterman, G.B., Frankenberg, C., Mandrake, L., O'Dell, C.,
18 Ahonen, P. and Biraud, S.C.: A method for evaluating bias in global measurements of CO₂ total columns from space, Atmospheric
19 Chemistry and Physics, 11(23), 12317-12337, 2011.

20 Wunch, D., Wennberg, P.O., Messerschmidt, J., Parazoo, N.C., Toon, G.C., Deutscher, N.M., Keppel-Aleks, G., Roehl, C.M.,
21 Randerson, J.T., Warneke, T. and Notholt, J.: The covariation of Northern Hemisphere summertime CO₂ with surface temperature
22 in boreal regions. Atmospheric Chemistry and Physics, 13(18), 9447-9459, 2013.

23 Wunch, D., Wennberg, P. O., Osterman, G., Fisher, B., Naylor, B., Roehl, C. M., O'Dell, C., Mandrake, L., Viatte, C., Griffith,
24 D. W., Deutscher, N. M., Velazco, V. A., Notholt, J., Warneke, T., Petri, C., De Maziere, M., Sha, M. K., Sussmann, R.,
25 Rettinger, M., Pollard, D., Robinson, J., Morino, I., Uchino, O., Hase, F., Blumenstock, T., Kiel, M., Feist, D. G., Arnold, S. G.,
26 Strong, K., Mendonca, J., Kivi, R., Heikkinen, P., Iraci, L., Podolske, J., Hillyard, P. W., Kawakami, S., Dubey, M. K., Parker,
27 H. A., Sepulveda, E., Rodriguez, O. E. G., Te, Y., Jeseck, P., Gunson, M. R., Crisp, D., and Eldering, A.: Comparisons of the
28 Orbiting Carbon Observatory-2 (OCO-2) XCO₂ measurements with TCCON, Atmos. Meas. Tech. Discuss., doi:10.5194/amt-
29 2016-227, in review, 2016.

Formatted: Font:Not Italic
Formatted: Font:Not Italic
Formatted: English (US)

Deleted:
Deleted: Toon, G. C., Wennberg, P. O., Wofsy, S. C.,
Stephens, B. B., Fischer, M. L., ... & Blavier, J. F
Formatted: English (US)

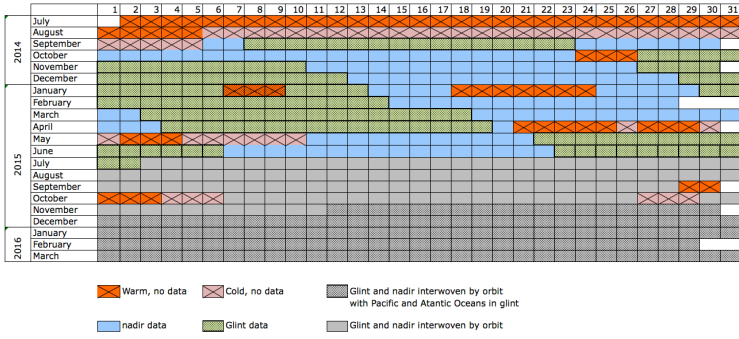
Deleted: Wennberg, P. O., Toon, G. C., Connor, B. J.,
Fisher, B., Osterman, G. B., ... & Biraud, S. C.:
Formatted: English (US)

Formatted: Font:(Default) Times New Roman, 12 pt, Not
Bold

Deleted: Wunch et al., Comparisons of the Orbiting
Carbon Observatory-2 (OCO-2) X_{CO2} measurements
with TCCON, submitted to Atmospheric Measurement
Techniques, 2016. .

1

2

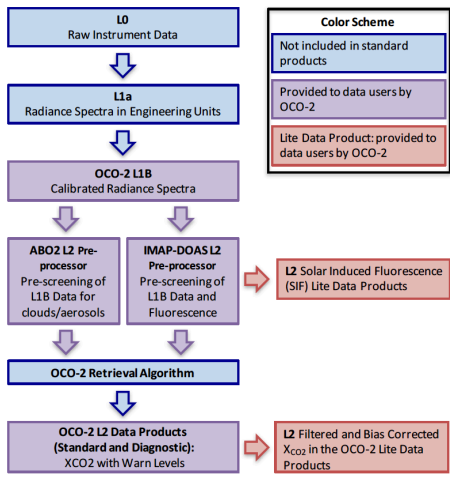


3

4

5 Figure 1. OCO-2 Data calendar with observation modes and data outages.

6

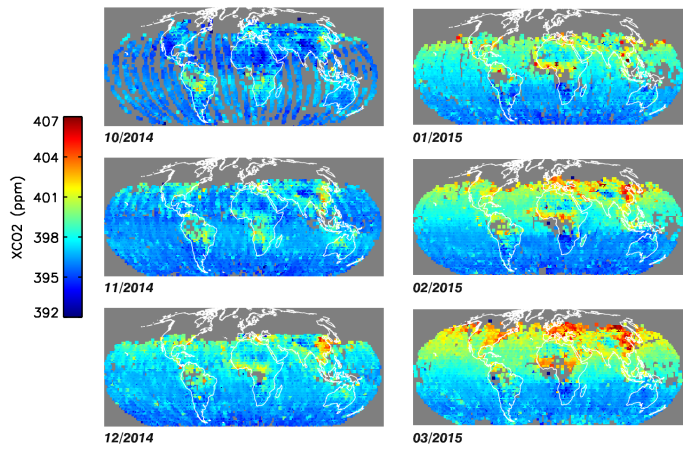


7

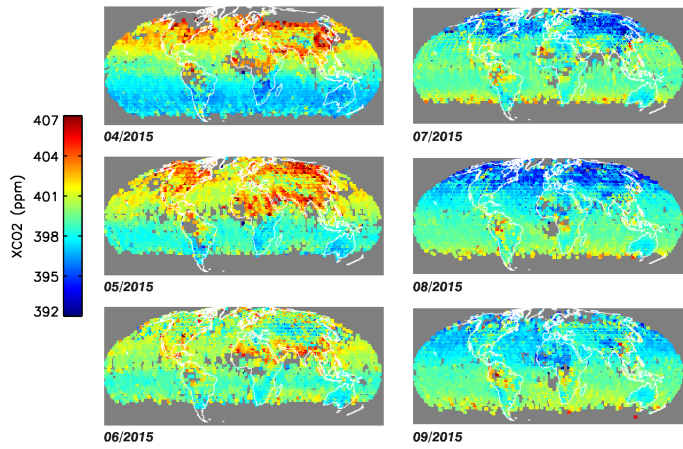
8 Figure 2. OCO-2 Data processing flow.

9

10

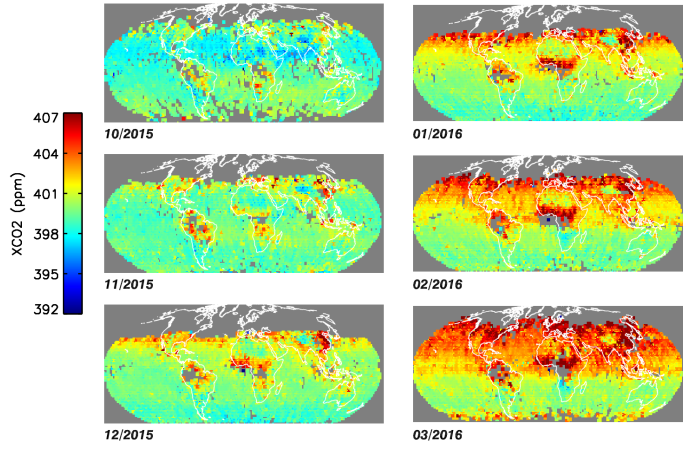


1
2
3 Figure 3. Maps of total column dry air ratio of CO₂ (X_{CO_2}) from OCO-2 from October 2014 through March 2015. Data has been
4 bias corrected and screened using the data quality flag in the Lite file, and averaged in 2 degree by 2 degree bins.



6
7 Figure 4. Maps of X_{CO_2} from OCO-2 from April 2015 through September 2015, bias corrected and selected with data quality flag
8 and averaged on 2 degree by 2 degree grid.

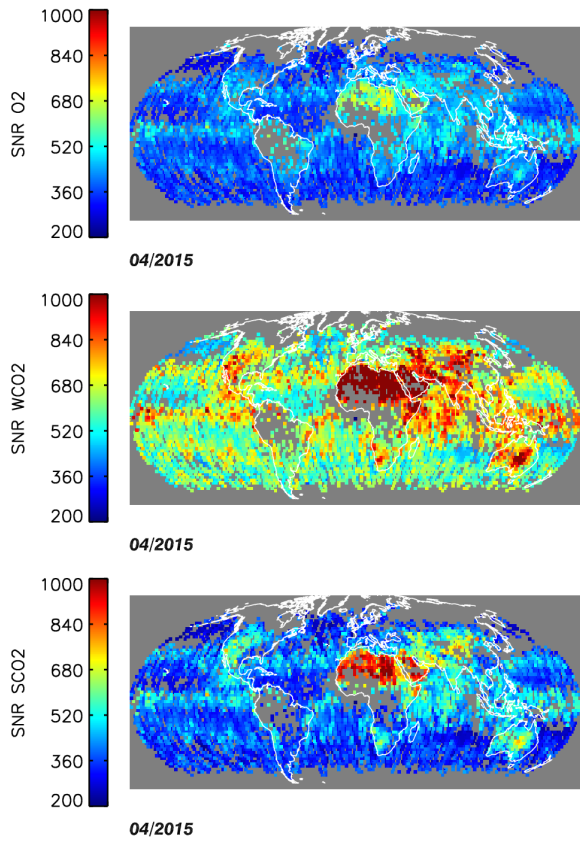
1



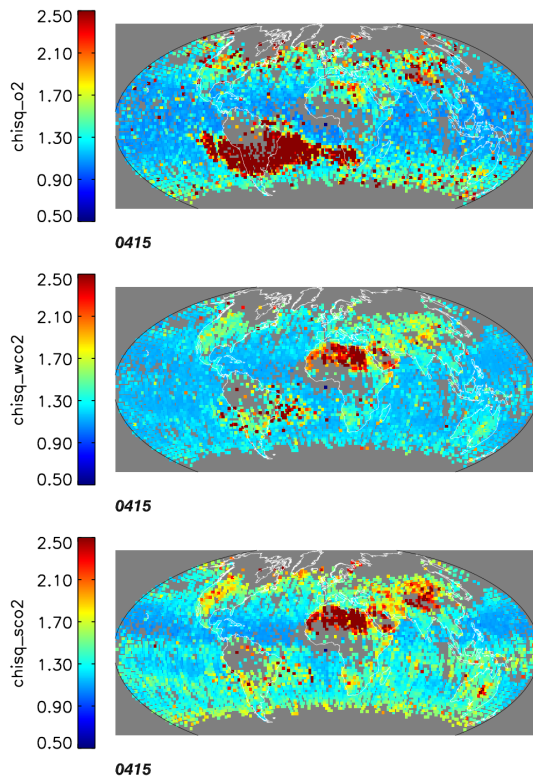
2

3 Figure 5. Maps of X_{CO2} from OCO-2 from October 2015 through March 2016, bias corrected and selected with data quality flag
4 and averaged on 2 degree by 2 degree grid.

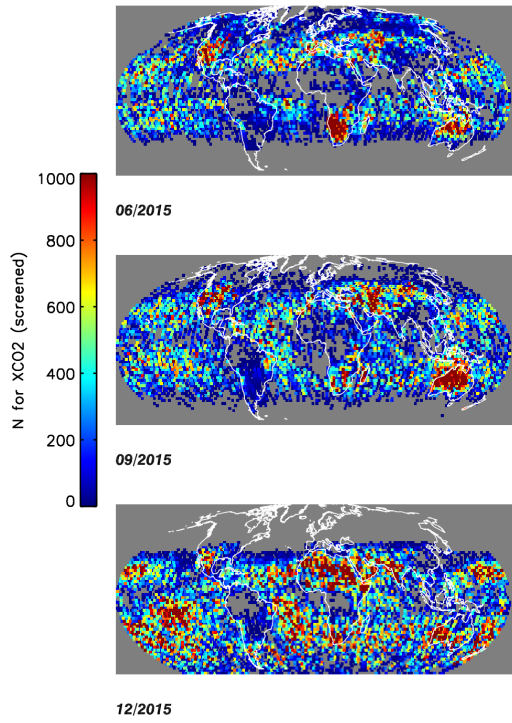
5



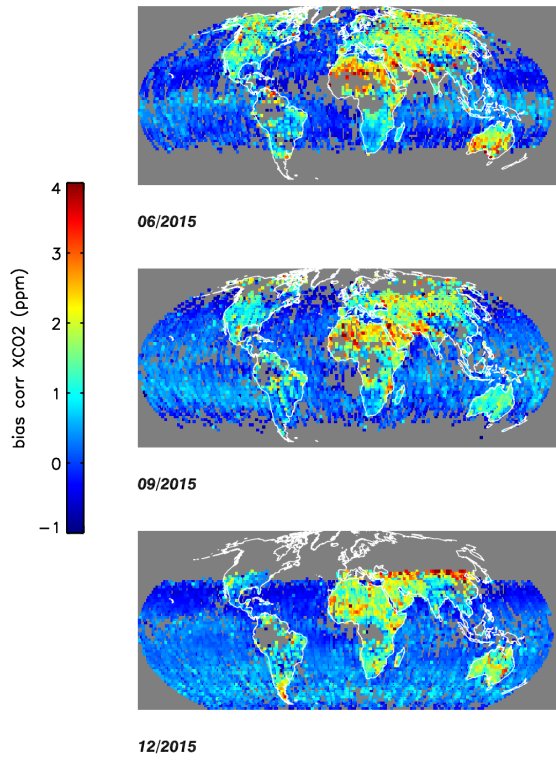
1
2 Figure 6. Maps of the continuum signal to noise ratio for the three bands of the OCO-2 instrument in April 2015. Statistics are
3 provided for 2 degree by 2 degree bins for data selected with the data quality flag.



1
 2 Figure 7. Maps of the fitting parameter χ^2 three bands of the OCO-2 instrument in April 2015. Statistics are provided for 2 degree
 3 by 2 degree bins for data selected with the data quality flag.
 4

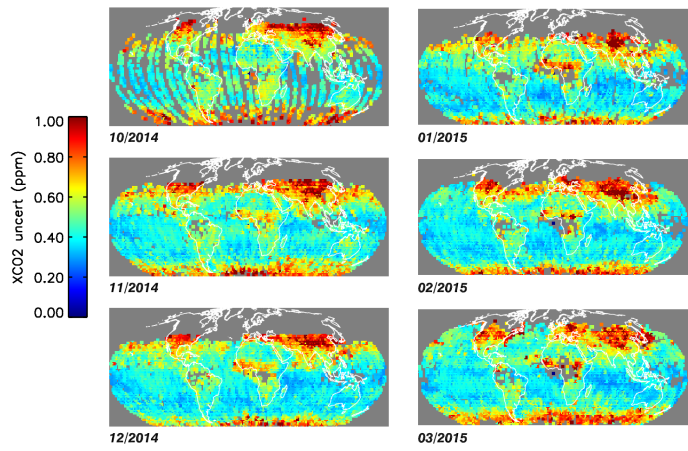


1
2 Figure 8. Maps of the number of soundings passing quality flagging for a selection of months. Statistics are provided for 2 degree
3 by 2 degree bins for data selected with the data quality flag.
4

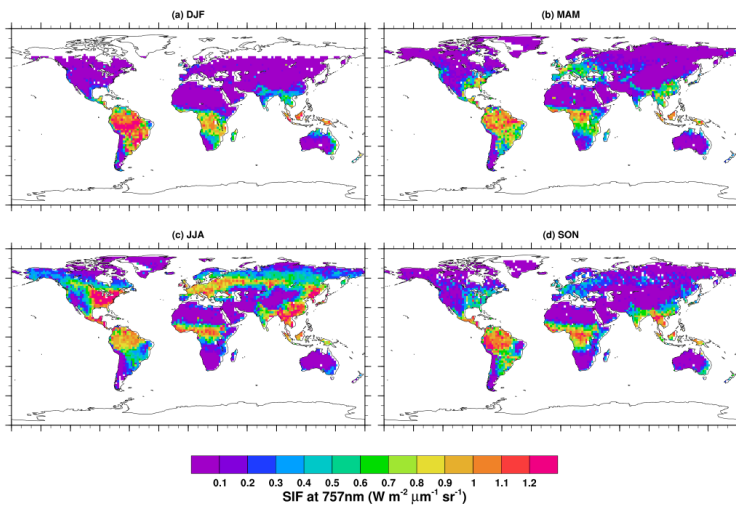


1
 2 Figure 9. Maps of the bias correction applied to the X_{CO_2} data. Statistics are provided for 2 degree by 2 degree bins for data selected
 3 with the data quality flag.

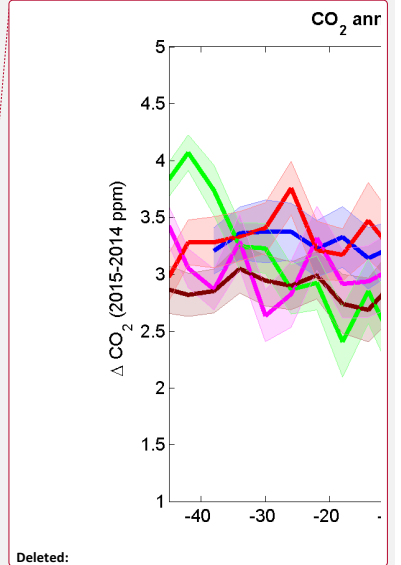
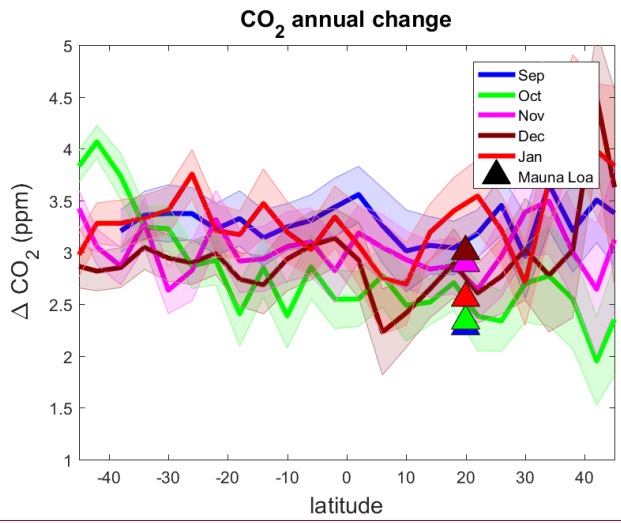
4
 5



1
2 Figure 10. Maps of the average X_{CO2} uncertainty in the OCO-2 data product. Statistics are provided for 2 degree by 2 degree bins
3 for data selected with the data quality flag.
4

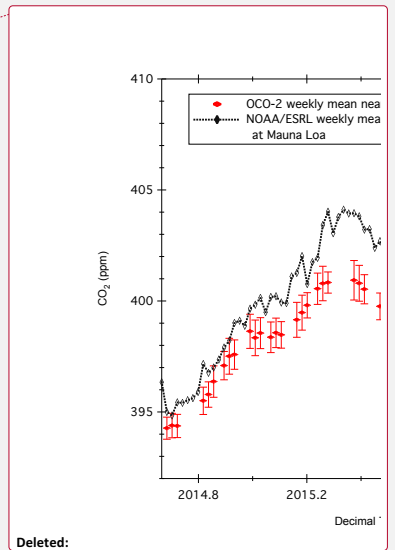


1
 2 Figure 11 – OCO-2 Solar Induced Fluorescence (SIF) product averaged on 2 degree by 2 degree grid for 3 month periods (December
 3 2014 through November 2015).
 4
 5

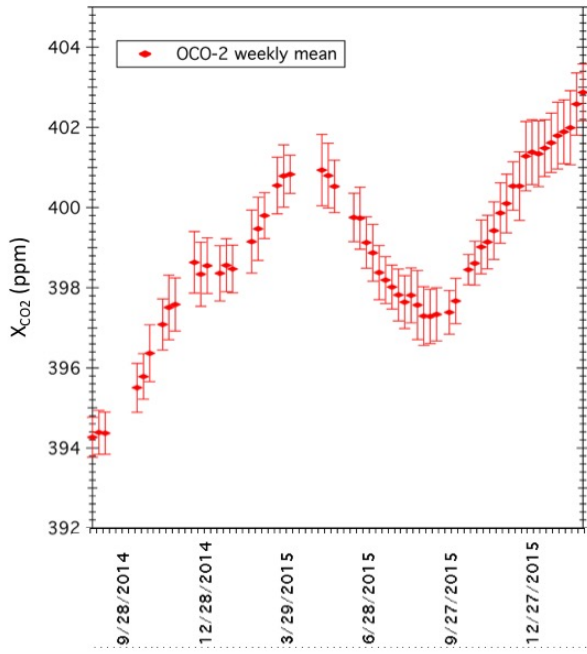


Deleted:

1
 2 Figure 12. Annual change of X_{CO2} zonal means from OCO-2 observations (lines) and from in situ measurements at Mauna Loa,
 3 Hawaii (triangles), plotted in different colors for the different months of measurements. Differences are between 2015 and 2014,
 4 except for January, which is January 2016 – January 2015. The shaded areas represent the standard deviations.



Deleted:

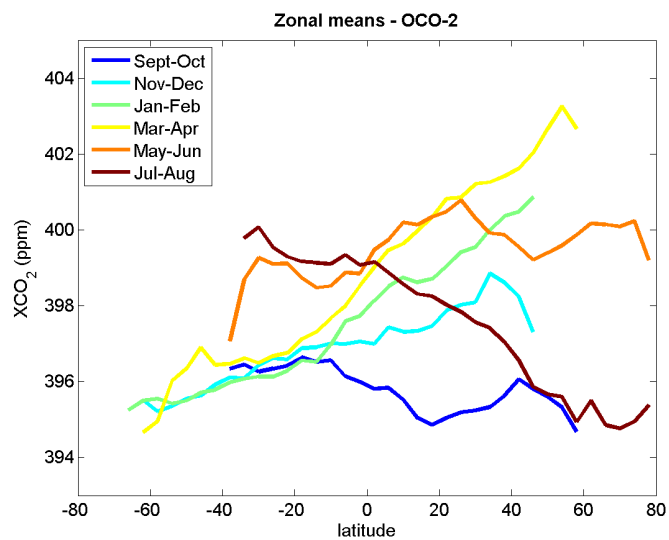


Formatted: Centered

1
 2 Figure 13 – Time series of weekly average OCO-2 X_{CO_2} measurements near Hawaii. Glint water measurements selected with the
 3 data quality flag from the Lite files.

Deleted: NOAA ESRL Mauna Loa Observatory weekly average CO_2 concentrations are overplotted in a black dashed line

4
 5



1

2 Figure 14: Latitudinal gradient for 2 month averages of OCO-2 X_{CO2} data between September 2014 and August 2015. All modes
 3 are averaged together in these figures.

4

5

Latitudinal gradient

The OCO-2 record adds additional detail to our understanding of the latitudinal gradients of X_{CO_2} . Figure 14 shows the zonal means of quality flagged OCO-2 X_{CO_2} data. As expected, there is a complete reversal of the latitudinal gradient between Northern Hemisphere spring and Northern Hemisphere summer. We see the contrast of the March-April 2015 gradient, where the Northern Hemisphere has X_{CO_2} concentrations 4 to 7 ppm larger than the Southern Hemisphere, whereas the reverse is seen in July - August. The southern hemisphere gradient is similar from September through April. The seasonal change of latitudinal coverage is also apparent in this plot, driven by both solar geometry and clouds, as discussed earlier. Wunch et al. (2016) shows comparisons of the latitudinal gradients as observed by OCO-2 and TCCON.